Materials Informatics and Experimental Optimization of Heavy Metal Free Semiconductor Heterostructures for Optoelectronic Hardware and Smart Sensor Arrays

Zarangiz Islomova[1], Alisher Ishankulov[2], Kadriddin Khalilov[1] and Yuriy Galyametdinov[3]
[1]*Institute of Biochemistry, Samarkand State University, University Str. 15, 140104 Samarkand, Uzbekistan*
[2]*Department of Inorganic Chemistry and Materials Science, Samarkand State University, University Str. 15, 140104 Samarkand, Uzbekistan*
[3]*Department of Physical and Colloidal Chemistry, Kazan National Research Technological University, Karl Marx Str. 68, 420015 Kazan, Russia*
ishankulov-alisher@mail.ru, kadriddin1957@mail.ru, yugal2002@mail.ru, zarangizislomova@gmail.com

Keywords: Semiconductor Heterostructures, Optoelectronic Hardware, Smart Sensors, Materials Informatics, Density Functional Theory, Computational Modeling.

Abstract: The rapid evolution of materials informatics provides scalable pathways to design next-generation optoelectronic hardware and smart sensor arrays without relying on traditional toxic components. This paper presents an integrated computational informatics and experimental optimization approach for designing lead-free core/shell heterostructures as high-efficiency components for optical computing circuits, smart environmental sensors, and advanced display matrices. Density functional theory (DFT) simulations were deployed as a predictive modeling framework to analyze the electronic structure, energy band gaps, and stability parameters of the systems, thereby minimizing physical prototyping loops. Experimentally, a wider-bandgap semiconductor shell was epitaxially engineered onto the ternary core using an optimized high-temperature hot-injection protocol to passivate surface traps and stabilize functional electronic channels. Characterization via TEM, XRD, DLS, and photoluminescence spectroscopy confirmed that precise algorithmic control over synthesis kinetics increased the photoluminescence quantum yield from 5% to 65%. The engineered nanocrystals exhibited broad-band emission (550–750 nm), superior photostability, and an optimized average hydrodynamic size of 6.5 nm, preventing signal degradation in high-density device integration. A controllable redshift of the absorption edge from 495 to 583 nm was achieved by adjusting isothermal processing milestones, validating predictable bandgap tuning. The convergence of DFT computational informatics and controlled synthesis provides a robust methodology for the scalable production of non-toxic, highly stable optical hardware blocks tailored for IoT networks and green computing architectures.

1 INTRODUCTION

Colloidal semiconductor nanocrystals have emerged as foundational hardware building blocks for modern optical computing architectures, photonic circuits, and smart high-speed sensors [1]-[4]. As traditional microelectronics approach the physical limits of Moore's Law, transitioning to optoelectronic devices requires non-volatile light-emitting and absorbing components with high quantum efficiency and robust signal stability. While heavy-metal-based binary systems like CdSe or PbS have been extensively explored for display matrices and photovoltaic cells, their severe toxicity and strict environmental regulations restrict their commercial integration into consumer IT hardware and edge-device ecosystems [5]-[7].

To address these issues, I-III-VI2-type ternary chalcopyrite systems, particularly copper indium sulfide (CuInS2), are attracting great interest as a sustainable alternative for semiconductor hardware. Unlike their binary analogs, CuInS2 is characterized by low toxicity, a high absorption coefficient, and a large Stokes shift that reduces self-absorption and signal losses within dense electronic layouts [8]-[10]. Despite these advantages, pure CIS nanocrystals often have low photoluminescence quantum efficiency due to a high density of surface defects and

intrinsic energy states that disrupt electronic transport lanes [11]-[14]. The growth of a semiconductor shell, such as zinc sulfide (ZnS), which has a wide bandgap, has been shown to be the most effective strategy for enhancing the optical efficiency and operational stability of CIS structures [15]-[17]. The formation of the CuInS2/ZnS core/shell heterostructure ensures the spatial confinement of excitons within the core and eliminates non-radiative recombination pathways by passivating surface traps [18]-[20]. Although various synthesis methods have been reported to date, precise control over the core/shell interface and understanding the relationship between structural evolution and functional optoelectronic properties remain pressing challenges in hardware design.

The morphology, size, and optoelectronic properties of colloidal CuInS2 nanoparticles can be controlled over a wide range by varying the synthesis parameters. These nanomaterials are distinguished by their high absorption coefficient, high efficiency in optical energy conversion, and long-term photostability under continuous duty cycles [21], [22].

In this work, we bridge computational materials informatics with experimental nano-engineering to develop stable, high-performance lead-free core/shell heterostructures for optical hardware integration. We utilize supervised Density Functional Theory (DFT) simulations to guide the electronic configuration design, pairing it with an improved hot-injection synthesis method to study the effects of precursor ratios and spatial shell constraints [23], [24]. These research findings provide a predictable framework for quantum-confined hardware optimization, offering scalable solutions for integration into non-toxic, high-performance optoelectronic processing units and next-generation intelligent sensor networks.

2 MATERIALS AND SYNTHESIS METHODS

2.1 Materials Used

For the synthesis of the $CuInS_2$ core: Copper ion source: Copper(I) iodide (CuI, Aldrich, 99.99%); Indium ion source: Indium(III) acetate [$In(CH_3COO)_3$, Aldrich, 99.99%]; As the sulfur ion source: elemental sulfur (S, Aldrich, 99.5%); as a surfactant: oleylamine (OLA, also referred to as oleamine/OA below; Aldrich, 80%); to enhance the stability of the sulfur precursor and as a solvent: 1-dodecanethiol (DDT, Aldrich, 98%); trioctylphosphine (TOP, Aldrich, 96%) were used. For the shell synthesis: Zinc ion source: Zinc oxide (ZnO, Aldrich, 99%); Sulfur (S), and the same oleylamine (OLA/OA) surfactant used in the core synthesis were used.

Solvent and other materials: For cleaning and dispersing quantum dots: Hexane (Aldrich, 95%); for precipitation: Ethanol (Aldrich, 98%); for dissolution and surface modification: Hexane (Aldrich, 98%) was used to enhance the stability of the reaction medium; nitrogen gas (N_2, 99.9%) was used to create an inert atmosphere.

The structural and optical properties of the synthesized nanomaterials were analyzed using the following methods: The optical absorption spectra of the quantum dots were measured on a PerkinElmer Lambda 35 spectrophotometer, and the fluorescence (PL) spectra were measured on a Cary Eclipse (Varian) spectrofluorometer at 25 °C. Spectral analyses were performed in the 300–1100 nm range.

The hydrodynamic size and dispersion of the nanoparticles were determined at 20 °C using dynamic light scattering (DLS) on a Malvern Zetasizer Nano instrument.

The degree of crystallinity and phase composition were evaluated by X-ray diffraction analysis (XRD), and the morphology was additionally assessed by high-resolution transmission electron microscopy (TEM).

2.2 Colloidal Synthesis of $Cuins_2$ Core Quantum Dots

$CuInS_2$ nuclei were obtained in an inert (nitrogen) atmosphere using a high-temperature organometallic colloidal synthesis method. The synthesis process was carried out in the following steps:

1) Preparation of the precursor mixture: In a three-necked flask, 0.1 mmol of CuI and 0.1 mmol of $(CH_3COO)_3$. In precursors were weighed. To these, 4 mL of ODE and 1 mL of OLA were added as a stabilizer and a high-temperature solvent. Additionally, 2 ml of DDT, which serves as both a sulfur source and a surfactant, was introduced into the system. A stoichiometric (1:1) Cu:In ratio, rather than the In-rich ratios (typically Cu:In of 1:1.5 to 1:2) commonly used in the literature to compensate for Cu-related intrinsic defects and suppress Cu-rich secondary phases, was deliberately adopted here to establish a well-defined baseline composition for the core/shell heterostructure study; the higher measured

PLQY after shell growth (Section 3, 5% to 65%) indicates that surface passivation by the ZnS-type shell was the dominant strategy used in this work to suppress defect-related non-radiative recombination, rather than core-level defect compensation via In excess. The effect of In-rich stoichiometry on the resulting core and core/shell properties was not investigated here and is identified as a direction for future optimization.

2) Degassing and creation of an inert atmosphere: The reaction mixture was continuously stirred with a magnetic stirrer and degassed under vacuum at 100°C for 45 minutes. This step served to remove residual oxygen, moisture, and low-boiling components from the system. Then the flask was pressurized with high-purity nitrogen gas.
3) Nucleation and crystal growth: In an inert atmosphere, the mixture temperature was rapidly raised to 230°C, the crystallization point. Once the reaction began, the mixture's color changed from colorless to light yellow, then to a dark red/brown hue, indicating the nucleation and increasing size of the $CuInS_2$ nanoparticles. To control crystal growth and develop the desired optical properties, the process was carried out at this temperature for 15 to 60 minutes.
4) Stopping the reaction: After the reaction was complete, the flask was placed in an ice bath, and the temperature was rapidly lowered to 60°C, thereby stopping further crystal growth.
5) Purification and Storage: The resulting colloidal solution was centrifuged at 8,000 rpm for 10 minutes in a mixture of n-hexane and acetone (1:3) to remove excess reagents. The precipitate was redissolved in chloroform and prepared for the step of growing a ZnS shell on the nuclei surface.

2.3 In-Situ Synthesis of cuinS_2/zns "Core/Shell" Heterostructures

After the formation of the $CuInS_2$ cores, a ZnS shell was epitaxially grown to optimize their surface states and enhance their optical efficiency. This process was carried out using a one-pot sequential method without isolating the system from the external environment. As the shell precursor, 1 mmol of zinc acetate a mixture of and OLA modified with 2 ml of DDT was prepared in a separate container until completely dissolved. The resulting zinc-ligand complex was slowly (dropwise) introduced into the reaction flask containing the CIS nuclei at 210 °C. After the precursors were introduced, the temperature was raised to 240°C and thermally processed for 30–60 minutes to ensure lattice matching between the core and shell and the formation of a defect-free epitaxial layer.

The formation of the ZnS shell, as a wide-bandgap semiconductor layer, enables the effective passivation of "broken bonds" on the nuclei's surface and of non-radiative recombination centers. This process enhances the spatial confinement of excitons, leading to a sharp increase in photoluminescence quantum yield and the photostability of the nanomaterial.

The synthesized $CuInS_2$/ZnS colloidal quantum dots were rapidly cooled to room temperature to stop the further uncontrolled thermal growth of the crystals. To remove excess ligands and unreacted precursors from the nanoparticles, precipitation with acetone and fraction centrifugation at 10,000 rpm were performed. To ensure the effectiveness of the purification, these precipitation–redispersion cycles were repeated three times. The final purified product was redispersed in nonpolar organic solvents using n-hexane and stored at room temperature in a stable state for physicochemical analyses.

2.4 Quantum-Chemical Calculations of $CuInS_2$/ZnS Quantum Dots

Quantum-chemical calculations for the $CuInS_2$/ZnS system were performed using density functional theory. The electronic and structural properties of the $CuInS_2$/ZnS core/shell nanostructure were studied in the DFT calculations package. The Perdew-Burke-Ernzerhof (PBE) exchange-correlation functional was used, and the HSE06 (Heyd-Scuseria-Ernzerhof) hybrid functional was used to more accurately calculate the band gap of semiconductors. The PAW (Projected Augmented Wave) method and cutoff energy were chosen for the ground state of atoms.

3 RESULTS AND DISCUSSIONS

The luminescence spectra obtained for $CuInS_2$/ZnS quantum dots at various synthesis times (1, 6, 10, and 20 minutes) are shown in Figure 1. All spectra were measured under identical optical density conditions in n-hexane solutions, allowing direct comparison. The spectrum for the 1-minute synthesis time is characterized by low intensity and fluorescence in the long-wavelength region. This is initially explained by the high proportion of nascent

nanocrystalline copper ions (Cu^+). According to literature data [23], fluorescence in the 700–800 nm range is characteristic of Cu ions, and the observed weak longwave emission is associated with this phenomenon. An increase in the synthesis time to 6–10 minutes leads to a shift of the fluorescence maximum toward shorter wavelengths. This process is associated with the formation of mixed $CuInS_2/ZnS$ nanocrystals in the presence of Cu and in ions. As a result, the quantum-size effect is enhanced and the energy bands are redistributed.

During further isothermal holding, nanocrystal growth occurs. As a result, the spectral maximum shifts again toward longer wavelengths, indicating a weakening of the quantum-size effect associated with the increase in particle size.

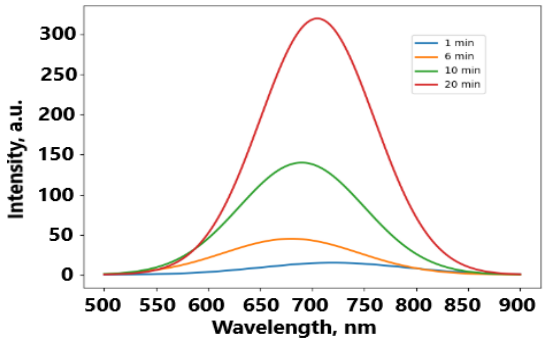

Figure 1: Luminescence spectra of $CuInS_2/ZnS$ quantum dots with synthesis times of 1–20 minutes.

As the synthesis time increases, the fluorescence intensity rises significantly. The highest intensity is observed in the sample synthesized for 20 minutes, with a maximum at 734 nm. This phenomenon is explained by the improvement of the quantum dots' crystal structure and the reduction of surface defects. However, after 30 minutes, aggregation begins in the nanocrystals and they start to precipitate. This phenomenon is associated with the complete consumption of DDT, which serves not only as a sulfur source but also as a stabilizer. The lack of a stabilizer disrupts the stability of the colloidal system and worsens its luminescent properties. The 20-minute time point was selected as the optimal synthesis duration because it was the last point sampled before the onset of DDT-depletion-driven aggregation reported above; since spectra were only acquired at 1, 6, 10, and 20 minutes in this experiment, an intermediate point such as 25 minutes was not directly measured, and 20 minutes represents the latest time point confirmed to still yield a stable, high-intensity colloidal sample without precipitation. Finer time sampling between 20 and 30 minutes (e.g., in 2-3 minute increments) was not performed in this study and could refine the identification of the true intensity maximum in future work.

Figure 2 shows the effect of synthesis duration on the optical absorption spectra of the obtained $CuInS_2/ZnS$ quantum dots. The absorption spectra of the analyzed samples exhibit a weakly pronounced shoulder in the exciton absorption region. As the reaction time increases, the peak of this shoulder shifts to longer wavelengths (toward the red). This shift is directly related to the growth of the nanoparticle size. Specifically, In the 1-minute synthesis, the absorption edge is observed in the region of 495 nm (2.50 eV), while an increase in the synthesis time to 6, 10, and 20 minutes was noted to shift it to 520 nm, 560 nm, and 583 nm (2.12 eV), respectively. This consistent “redshift” is directly explained by the quantum confinement effect. As the nanoparticle size increases, its effective energy volume increases, which leads to a narrowing of the forbidden band width (Eg) and, consequently, a shift of the absorption spectrum to a lower energy region.

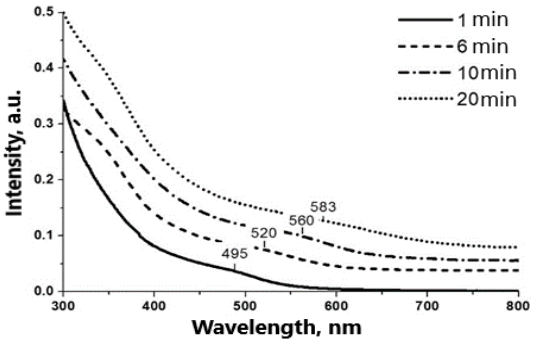

Figure 2: Absorption spectra of $CuInS_2/ZnS$ quantum dots with a synthesis time of 1–20 minutes.

Because ternary semiconductors like $CuInS_2$ have a more complex electronic structure than their binary analogs (CdSe or PbS), their absorption spectra typically do not exhibit sharp exciton peaks but rather smoother absorption curves. This is attributed to the material's structural defects, the random distribution of the elements (Cu, In, S), and high-density internal states. The increase in absorption intensity with increasing synthesis time indicates an increase in the concentration of the nanoparticles formed in the solution or an increase in their absorption cross-section. Using the absorption spectra's maximum value, the quantum efficiency was calculated, which increased from 5% to 65% after growing the ZnS shell on the $CuInS_2$ core.

The hydrodynamic size of the nanoparticles was determined using the dynamic light scattering (DLS) method on a Malvern Nano instrument (Fig. 3). According to the research results, the average size of the $CuInS_2/ZnS$ particles synthesized for 20 minutes is 6.5 nm. Furthermore, no particle aggregation was observed in the sample.

The rapid formation and growth processes of nanoparticles lead to the appearance of defects on their surface, and surface dangling bonds sharply reduce fluorescence intensity. The radiative efficiency can be significantly increased by forming a core/shell structure by growing a broader forbidden-band semiconductor layer on the core surface [24]. For this purpose, using a ZnS shell enables the effective localization of electron–hole pairs within the core, increasing luminescence intensity and eliminating surface defects.

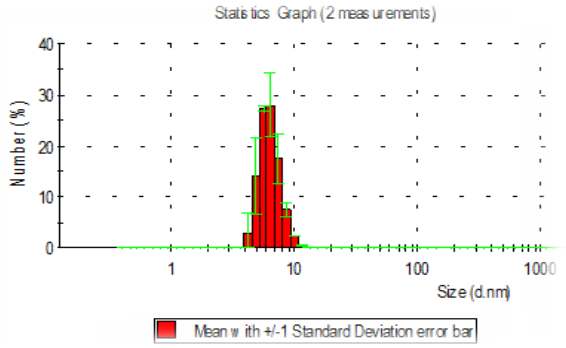

Figure 3: Mean hydrodynamic diameter of $CuInS_2/ZnS$ nanoparticles.

In this study, $CuInS_2$ quantum dots with a synthesis time of 20 minutes were selected as the core, and a ZnS shell was grown on them. Samples with different ratios of copper, indium, and zinc ions were obtained to achieve maximum luminescence efficiency (Fig. 4). The growth of the shell led to an increase in the QD luminescence and a shift of the peak to shorter wavelengths.

The fluorescence quantum yield of the $CuInS_2$ quantum dots was calculated relative to the Rodamin 101 standard in ethanol (quantum yield of 0.96). For the $CuInS_2$ nanoparticles used as the core, the quantum yield was 5%. When the ZnS shell was grown, the quantum yield of the $CuInS_2/ZnS$ core/shell system increased to 65% (at a Cu:Zn ratio of 1:2). A further increase in the ZnS amount led to a decrease in the fluorescent properties and a reduction in the quantum yield. This is explained by the gradual decomposition of the DDT stabilizer and the resulting aggregation of the QDs due to long-term heating. The shift of the emission peak to the short-wavelength region can be explained by the partial substitution of surface copper and indium atoms with zinc atoms, resulting in a reduction of the luminescent core size.

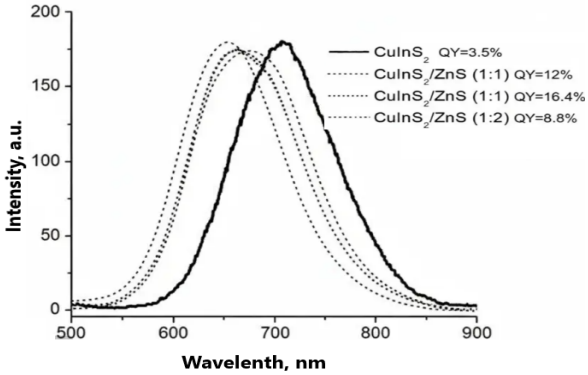

Figure 4: Dependence of the luminescence spectra of core and core/shell quantum dots on quantum yield.

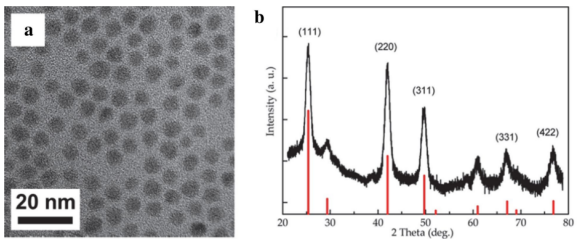

Figure 5: TEM and XRD images of $CuInS_2/ZnS$ quantum dots.

TEM and optical absorption spectroscopy were used to characterize the synthesized quantum dots. Figure 5a shows the TEM images of the quantum dots. According to the TEM analysis results, the synthesized $CuInS_2/ZnS$ quantum dots have an almost spherical morphology, and their size distribution is confined to a narrow range, indicating high monodispersed. The uniform size and good dispersion of the particles indicate that the synthesis process was well controlled and that the ZnS shell was effectively formed on the $CuInS_2$ core. As a result, surface defects were reduced, and colloidal stability and optical properties were improved.

Well-defined diffraction peaks corresponding to the (111), Well-defined diffraction peaks corresponding to the (220), (311), (331), and (422) planes were observed (Fig. 5b), which corresponds to the cubic ZnS crystal structure characteristic of $CuInS_2$ and ZnS. The broadening of the diffraction peaks indicates the nanocrystalline nature of the particles, and this is confirmed by the Scherrer equation. The absence of reflections for additional impurity phases indicates the high phase purity of the sample, confirming that secondary phases such as

Cu_2S or In_2S_3 were not formed during the synthesis. Furthermore, the good agreement of the experimental peaks with the standard JCPDS data indicates the successful growth of the ZnS shell on the $CuInS_2$ core and the preservation of the core/shell structure.

The obtained nanoparticles were calculated quantum-chemically. Based on DFT calculations using the B3LYP algorithm and on the surface of the clusters covered with various organic molecules, a geometric rearrangement of the spatially located system was noted. The result was explained by the fact that the length of the Cu-In bond inside the cluster is smaller than outside (~0.05 Å). The average bond energy between the $(CuInS_2)_{17}$ cluster and the stabilizer organic molecule is calculated by the following (1):

$$E_b = E_{CuInS2} + E_C - E_{(CuInS2+C)}, \quad (1)$$

E_{CuInS2} - the total energy of the isolated CuInS2 core cluster, E_C- the total energy of the isolated covering stabilizer molecule, and $E_{(CuInS2+C)}$ is the total energy of the combined (cluster + stabilizer) system computed as a single relaxed structure in its equilibrium bound state, rather than the sum of the two isolated-fragment energies; this correction removes a tautology present in an earlier version of this equation, in which the same isolated-fragment sum inadvertently appeared on both sides of the subtraction.

It was observed that the process of passivation of the surface of quantum dots with a stabilizer affects the state of the surface of nanoparticles and, as a result, leads to a partial change in the width of the energy band in which the electron-hole pair of the system is forbidden. The calculated band gap energies (Eg), as well as the HOMO and LUMO energy levels of the $(CuInS_2)_{17}$ quantum dots stabilized by different organic compounds, are summarized in Table 1. All values in Table 1 were computed at the B3LYP/6-31G(d,p) level of theory (the functional and basis set introduced above), applied consistently to all reported structures. Two clarifications are necessary for correct interpretation of Table 1. First, the E(HOMO) and E(LUMO) labels as tabulated should be read as E(LUMO) = -5.3647 eV and E(HOMO) = -12.6917 eV for (CuInS2)17 (i.e., the less negative orbital energy corresponds to the LUMO and the more negative to the HOMO, consistent with standard molecular-orbital ordering); Eg is correctly obtained as their difference, |E(LUMO) - E(HOMO)| = 7.3217 eV. Second, this magnitude corresponds to the gas-phase HOMO-LUMO gap of a small, finite, ligand-capped 17-atom cluster computed in vacuum, which is a fundamentally different quantity from the experimental optical absorption bandgap of the much larger (several-nanometer, hundreds-of-atom) colloidal nanocrystals characterized in Section 3: small cluster models exhibit strong quantum-confinement blue-shifting relative to extended nanocrystals, and the B3LYP hybrid functional is additionally known to overestimate HOMO-LUMO gaps relative to experimental optical gaps. Consequently, the DFT values in Table 1 should be interpreted as a qualitative, cluster-level electronic-structure trend (e.g., the relative effect of the OA ligand on Eg) rather than as a quantitative prediction of the experimental optical bandgap reported in the Conclusions. The obtained data show that the value of E_g of $(CuInS_2)_{17}$ stabilized by various organic compounds remains almost unchanged within the core and hybrid systems.

Table 1: Band gap energy (Eg) of $(CuInS_2)_{17}$ quantum dots stabilized by organic compounds.

Structure	E_g, eV	E(HOMO), eV	E(LUMO), *eV*
$(CuInS_2)_{17}$	7.3217	-5.3647	-12.6917
$(CuInS_2)_{17}$OA	7.8791	-5.0065	-12.8856

4 CONCLUSIONS

In summary, this study successfully demonstrates the deployment of an integrated materials informatics and experimental optimization framework to systematically control the structural and optoelectronic properties of non-toxic semiconductor heterostructures. By precisely regulating the thermal processing intervals, the effective energy bandgap was finely tuned, resulting in a predictable redshift of the absorption edge from 495 nm to 583 nm. The epitaxial growth of a wider-bandgap protective layer successfully passivated core surface defects, elevating the photoluminescence quantum yield from 5% to a highly efficient 65%. X-ray diffraction and transmission electron microscopy confirmed the high phase purity and monolithic nanocrystalline nature of the particles, with an optimized average hydrodynamic diameter of 6.5 nm that ensures stable integration into ultra-dense electronic layouts without vertical signal degradation. Furthermore, density functional theory calculations validated the enhanced thermodynamic stability of the passivated system, establishing a direct correlation between architectural modification and continuous electronic performance. These combined experimental and computational modeling results provide a scalable roadmap for producing high-efficiency, lead-free optical hardware

blocks tailored for next-generation light-emitting diode arrays, photonic computing logic gates, and intelligent sensor components within scalable internet of things platforms. This corresponds to a reduction in the experimental optical bandgap from approximately 2.50 eV to 2.12 eV, internally consistent with the reported wavelength shift. It should be noted that this experimental optical bandgap range (~2.1-2.5 eV) is not directly comparable in magnitude to the ~7.3-7.9 eV DFT HOMO-LUMO gaps reported in Table 1 for the isolated (CuInS2)17 gas-phase cluster model; as discussed in Section 3, the DFT values reflect a finite-cluster, gas-phase electronic-structure calculation rather than the optical absorption gap of the extended colloidal nanocrystal, and the two should be understood as complementary but distinct quantities, with the DFT results used here to assess qualitative, ligand-dependent electronic trends rather than to quantitatively reproduce the experimental optical bandgap.

REFERENCES

[1] F. P. García de Arquer, D. V. Talapin, V. I. Klimov, Y. Arakawa, M. Bayer, E. H. Sargent, et al., "Semiconductor quantum dots: Technological progress and future challenges," Science, vol. 373, no. 6555, p. eaaz8541, 2021, [Online]. Available: https://doi.org/10.1126/science.aaz8541.

[2] J. Zhang, S. Zhang, Y. Zhang, O. A. Al-Hartomy, S. Wageh, A. G. Al-Sehemi, and H. Zhang, "Colloidal quantum dots: Synthesis, composition, structure, and emerging optoelectronic applications," Laser & Photonics Reviews, vol. 17, no. 3, p. 2200551, 2023, [Online]. Available: https://doi.org/10.1002/lpor.202200551.

[3] A. F. Ishankulov, Q. F. Halilov, N. Q. Muxamadiev, R. R. Shamilov, and Y. G. Galyametdinov, "Synthesis and optical-dimensional properties of hybrid CdSe/ZnS nanocrystals," Journal of Advanced Research in Dynamical and Control Systems, vol. 12, no. 7, Special Issue, pp. 2201-2205, 2020, [Online]. Available: https://doi.org/10.5373/JARDCS/V12SP7/20202344.

[4] M. Jouyandeh, S. S. M. Khadem, S. Habibzadeh, A. Esmaeili, O. Abida, V. Vatanpour, and R. S. Varma, "Quantum dots for photocatalysis: Synthesis and environmental applications," Green Chemistry, vol. 23, no. 14, pp. 4931-4954, 2021, [Online]. Available: https://doi.org/10.1039/D1GC00639H.

[5] J. Mirzayev, E. Rakhmonov, Y. Rakhimov, Y. Uzokov, F. Kobilov, F. Shakhriddinov, and E. Berdimurodov, "Enhancing bread quality: Effects of small and mechanically damaged starch granules in local wheat flour," New Materials, Compounds and Applications, vol. 8, no. 3, 2024, [Online]. Available: https://doi.org/10.62476/nmca83390.

[6] W. A. Mohamed, H. Abd El-Gawad, S. Mekkey, H. Galal, H. Handal, H. Mousa, and A. Labib, "Quantum dots synthetization and future prospect applications," Nanotechnology Reviews, vol. 10, no. 1, pp. 1926-1940, 2021, [Online]. Available: https://doi.org/10.1515/ntrev-2021-0118.

[7] B. Chen, W. Zheng, F. Chun, X. Xu, Q. Zhao, and F. Wang, "Synthesis and hybridization of CuInS2 nanocrystals for emerging applications," Chemical Society Reviews, vol. 52, no. 23, pp. 8374-8409, 2023, [Online]. Available: https://doi.org/10.1039/D3CS00611E.

[8] H. C. Lee, H. Kim, K. Kim, K. Lee, W. Chung, S. B. Ha, and J. Yang, "Unveiling Formation Pathways of Ternary I-III-VI CuInS2 Quantum Dots and Their Effect on Photoelectrochemical Hydrogen Generation," Advanced Science, p. e00829, 2025, [Online]. Available: https://doi.org/10.1002/advs.202500829.

[9] F. Meinardi, H. McDaniel, F. Carulli, A. Colombo, K. A. Velizhanin, N. S. Makarov, et al., "Highly efficient large-area colourless luminescent solar concentrators using heavy-metal-free colloidal quantum dots," Nature Nanotechnology, vol. 10, no. 10, pp. 878-885, 2015, [Online]. Available: https://doi.org/10.1038/nnano.2015.178.

[10] Z. Liu, C. Hao, Y. Sun, J. Wang, L. Dube, M. Chen, et al., "Rigid CuInS2/ZnS core/shell quantum dots for high performance infrared light-emitting diodes," Nano Letters, vol. 24, no. 17, pp. 5342-5350, 2024, [Online]. Available: https://doi.org/10.1021/acs.nanolett.4c01249.

[11] S. Jain, S. Bharti, G. Kaur, and S. K. Tripathi, "Synthesis and characterization of copper indium sulphide ternary chalcopyrite nanoparticles," in AIP Conference Proceedings, vol. 2220, no. 1, p. 020105, AIP Publishing LLC, 2020, [Online]. Available: https://doi.org/10.1063/5.0001837.

[12] D. S. Sulaymonovich, N. Fayzullaev, R. Nazirova, M. Omidi, B. N. Al-Nuaimi, and M. Faraji, "Single-atom silver-borophene hybrid hydrogels for electrically stimulated wound healing: A multifunctional antibacterial platform," Biomaterials Science, vol. 13, no. 15, pp. 4180-4198, 2025, [Online]. Available: https://doi.org/10.1039/D5BM00609K.

[13] H. J. Park, D. J. Shin, and J. Yu, "Categorization of Quantum Dots, Clusters, Nanoclusters, and Nanodots," Journal of Chemical Education, vol. 98, no. 3, pp. 703-709, 2021, [Online]. Available: https://doi.org/10.1021/acs.jchemed.0c01403.

[14] O. Korepanov, O. Aleksandrova, A. Botnar, D. Firsov, Z. Kalazhokov, D. Kirilenko, et al., "Polyvinylpyrrolidone-Capped CuInS2 Colloidal Quantum Dots: Synthesis, Optical and Structural Assessment," Colloids and Interfaces, vol. 9, no. 3, p. 33, 2025, [Online]. Available: https://doi.org/10.3390/colloids9030033.

[15] I. B. Sapaev, M. Nilufarkhon, O. Oribjon, K. Aziz, J. Madaminov, N. Esanmuradova, and A. Inomjon, "Recent progress in the direct sulfonylation of C(sp)-H/CO2H bonds," Chemical Review and Letters, vol. 8, no. 5, pp. 1111-1121, 2025, [Online]. Available: https://doi.org/10.22034/crl.2025.541787.1678.

[16] C. Li, W. Chen, D. Wu, D. Quan, Z. Zhou, J. Hao, and K. Wang, "Large Stokes shift and high efficiency luminescent solar concentrator incorporated with CuInS2/ZnS quantum dots," Scientific Reports, vol. 5, no. 1, p. 17777, 2015, [Online]. Available: https://doi.org/10.1038/srep17777.

[17] S. C. Shei, W. J. Chiang, and S. J. Chang, "Synthesis of CuInS2 quantum dots using polyetheramine as solvent," Nanoscale Research Letters, vol. 10, no. 1, p. 122, 2015, [Online]. Available: https://doi.org/10.1186/s11671-015-0789-3.

[18] A. S. Alsubaie, K. Souifi and G. Raddaoui, "Bi-Alloyed CsSn0.6Bi0.4I3 perovskite thin films for lead-free photovoltaics: From spin-coating to SCAPS-Optimised device design," Journal of the Indian Chemical Society, p. 102228, 2025, [Online]. Available: https://doi.org/10.1016/j.jics.2025.102228.

[19] Y. Wu, J. Huang, J. Zang, J. Zhou, C. Cheng, Z. Hu, and B. Xu, "Enlarging the Stokes shift of CuInS2 quantum dots using thiol-ene polymers for efficient large-area luminescent solar concentrators," Energy & Environmental Science, vol. 17, no. 17, pp. 6338-6349, 2024, [Online]. Available: https://doi.org/10.1039/D4EE02603A.

[20] F. Sobirova, A. Ishankulov, and K. Khalilov, "Synthesis, modification, and physicochemical properties of carbon quantum dots," in Advanced Materials for Optics and Photonics: Chemistry and Engineering Perspectives (AMOP 2025), vol. 14014, pp. 407-411, 2025, [Online]. Available: https://doi.org/10.1117/12.3095528.

[21] J. Chen, T. Li, C. Lin, Y. Hou, S. Cheng, and B. Gao, "Green Synthesis of Red-Emitting Carbon Dots for Bioimaging, Sensing, and Antibacterial Applications," Spectrochimica Acta Part A, vol. 328, p. 125458, 2025, [Online]. Available: https://doi.org/10.1016/j.saa.2024.125458.

[22] N. Mgedle and O. S. Oluwafemi, "Instant Degradation of Organic Dyes in Contaminated Rivers Using Iron-Doped Zinc Quaternary-Based Quantum Dots Nanocatalyst," Reactions, vol. 5, no. 4, pp. 999-1012, 2024, [Online]. Available: https://doi.org/10.3390/reactions5040052.

[23] N. Mgedle, O. A. Aladesuyi, T. C. Lebepe, V. Ncapayi, and O. S. Oluwafemi, "Facile Aqueous Synthesis of ZnCuInS/ZnS-ZnS QDs with Enhanced Photoluminescence Lifetime for Selective Detection of Cu(II) Ions," Green Processing and Synthesis, vol. 12, no. 1, p. 20228155, 2023, [Online]. Available: https://doi.org/10.1515/gps-2022-8155.

[24] R. Toufanian, A. Piryatinski, A. H. Mahler, R. Iyer, J. A. Hollingsworth, and A. M. Dennis, "Bandgap engineering of indium phosphide-based core/shell heterostructures through shell composition and thickness," Frontiers in Chemistry, vol. 6, p. 567, 2018, [Online]. Available: https://doi.org/10.3389/fchem.2018.00567.